

# OPTIMIZATION OF MULTI-MATERIALS IN-FLIGHT MELTING IN LASER ENGINEERED NET SHAPING (LENS) PROCESS

Jingyuan Yan<sup>1</sup>, Ilenia Battiato<sup>2</sup>, and Georges M. Fadel<sup>1</sup>

<sup>1</sup>Department of Mechanical Engineering, Clemson University, Clemson, SC 29634

<sup>2</sup>Department of Mechanical Engineering, San Diego State University, San Diego, CA 92182

REVIEWED

## **Abstract**

A heterogeneous object has potentially many advantages and in many cases can realize appearance and/or functionality that homogeneous objects cannot achieve. LENS<sup>TM</sup>, a Direct Metal Deposition process, is one technology with the potential to fabricate heterogeneous objects. In-flight melting provides an advantageous condition for better mixing of multiple materials with different properties, thus critical for fabricating heterogeneous objects. In this study, a multi-materials in-flight melting model of the LENS process is developed for the cases of single and multiple particles jets. The impact of in-flight particles melting as well as substrate melting on materials mixing is investigated. An optimization method is proposed for the LENS fabrication of heterogeneous objects based on the concurrent melting of particles and substrate. A cermet composite material fabrication test case is utilized to demonstrate the applicability of the method. Inconel 718 powders and alumina ceramic powders are used as building materials in the test case. A group of optimized process parameters are provided: using a 320 W, 600  $\mu\text{m}$  spot diameter laser moving at 10 mm/s, the injection angles are 20°, the injection velocities are 1 m/s, the material feeding rates are 0.5 g/min, the particle diameters are 20  $\mu\text{m}$ , and the nozzle diameters are 0.7 mm for both materials. Moreover, the material with a lower melting point should be injected in the front of the laser moving direction, while the material with a higher melting point should be injected from the rear.

## **1. Introduction**

A heterogeneous object or component refers to an object with spatially distributed different material composition or structures [1]. It can be composed of different materials (or phases) with different properties, similarly to a composite, or the same material in different states, such as a polycrystal [2]. For instance, the make of functionally graded material (FGM) can enable different physical properties within a single object. The concept of heterogeneous object has been widely studied in engineering. Generally, heterogeneous objects can be categorized into three types: multi-material objects with clear material boundaries such as fiber resin composites, FGM objects with continuously varying material composition, and heterogeneous materials consisting of freely distributed materials [3]. The fabrication of the third type of heterogeneous objects is the focus of this paper.

A heterogeneous object has many advantages and can realize appearance and/or functionality that homogeneous objects cannot achieve, e.g. enhancement of the overall physical properties of the object, cost and weight reduction, avoiding any possible defects such as corrosion. Ever since 1980s when the concept of FGM was proposed [4], the potential

application of heterogeneous objects has been demonstrated in different engineering fields, including optic and electronic materials [4, 5], bioengineering [6, 7] and manufacturing of heterogeneous engineering parts such as flywheels [8, 9], injection molds [10], turbine blades [11], and cutting tools [12].

## **2. Manufacturing of heterogeneous object**

Heterogeneous objects can be manufactured via different processing techniques such as laser engineered net shaping (LENS<sup>TM</sup>) (also named as laser cladding), ultrasonic consolidation (UC) [13, 14], shape deposition manufacturing (SDM) [15, 16], selective laser sintering (SLS) [17, 18], thermal/plasma spraying [19]. Among the former, LENS is a flexible rapid prototyping method capable to fabricate dense metal/alloy parts, FGM and composite materials [20-22]. LENS also has superior versatility in component geometry compared to other rapid manufacturing techniques [20], and its process parameters can be tailored to achieve closed loop control for accurate part fabrication.

The coaxial LENS free form fabrication process generally consists of a continuous wave or pulsed [23, 24] laser inducing melt/plasma pool on the substrate, and (assembled) nozzles injecting powders into the melt pool in an inert environment. The basic schematic is shown in figure 1. Some variants may include an inner or outer extra shielding gas orifice [25-27]. The powders are fed by inert gas such as argon. The cladding forms as a result of the melt pool solidification, and the cladding is built up on the substrate with the relative movement between the laser and the substrate.

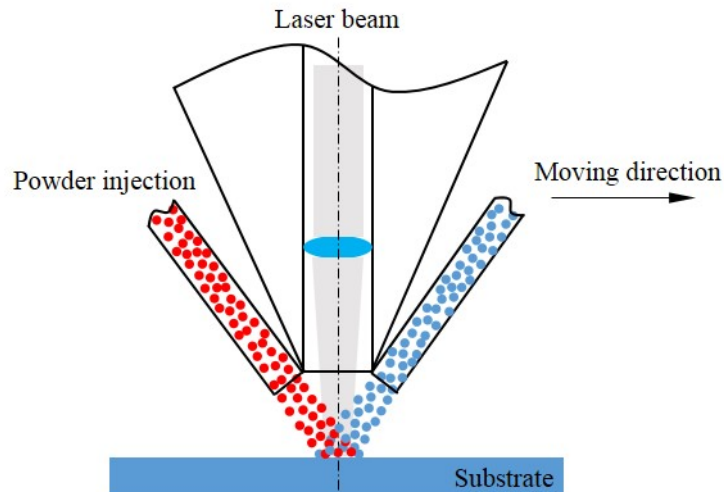


**Figure 1.** Schematic of the modified LENS process.

A wide range of different metals and alloys have been deposited by LENS, such as 316 SS [28, 29], NiTi [30], CoCrMo alloy [31], nickel based alloys like Inconel 625 [32, 33], and titanium based alloys like Ti-6Al-4V [34, 35]. A different approach consists in using elemental powder blends (i.e. premixed different powders) as feed powders. The premixed powders can be either alloys or pure metals [36-39]. As such, different phases can be generated during fabrication. This approach, however, lacks flexibility due to the fixed proportion of different

powders in the pre-blend mixture. Additionally, segregation effects in the blended powders due to powder density, size, shape and surface characteristics, render the quality of the fabricated objects hard to control. Another LENS-based approach consists in adding a mixer between the nozzle and the powder feeder [40], thus weakening the defect of segregation, and increasing the controllability of the process. Yet, the segregation effect cannot be completely removed. Moreover, the control of heating and deposition of different materials lacks flexibility.

A novel modified LENS technique, which allows different kinds of powders to be injected from different nozzles, has been demonstrated to have the potential to build heterogeneous objects in an “in situ” way, as shown in figure 1 [21, 26, 41]. A plate with transition from commercially pure titanium to 80Ti-20Nb alloy was built by Lewis et al. [41]. Liu et al. fabricated TiC/Ti composite material with compositions ranging from pure Ti to 95 vol% TiC [21]. Yakovlev et al. also built stellite and SS 316L composite structures [26]. This LENS approach adds materials where needed by process control, thoroughly eliminating the segregation in blended powders while decreasing stress concentration at the interface. However, the study of this “in situ” technique is limited to experiment, and, to the best of our knowledge, no studies have focused on the modeling and optimization of the LENS fabrication of heterogeneous objects.

The objective of this study is to model, and optimize the LENS process in heterogeneous objects fabrication. In section 3.1, we present the in-flight melting model of single particle and provide an analytical solution. In section 3.2, we study the shadowing effect of laser intensity due to particle clouds. We then apply our analysis to the fabrication of cermet composites and study substrate heating in section 3.3. Finite element simulation is applied to simulate the temperature profile on substrate. In section 4, we develop a process parameters optimization procedure in order for an optimal material fusion inside the melt pool, allowing particles and substrate to melt concurrently. Finally, the main results and conclusions are summarized in Section 5.

### **3. Model formulation of LENS process**

Laser material interaction consists of a series of coupled physical processes, including laser absorption, heat transfer, shock wave generation and propagation, vapor/plasma dynamics, melt pool dynamics, phase transition, and solidification [42-44]. In this study, a simplified thermal model is used to guarantee the concurrent melting of different particles as well as substrate surface at the designed spatial-temporal location, using Inconel 718 and ceramics as building materials for instance. The process parameters are specific to the LENS equipment of OPTOMECH MR-7 (OPTOMECH Inc., Albuquerque, NM).

#### **3.1 Modeling of the in-flight melting of single particle**

The in-flight melting is important for the fabrication of heterogeneous materials. In order to achieve good fusion inside of the melt pool, particles need to be melt as much as possible during the flight. Melted liquid particles would form a better fusion bonding with the melted substrate [25, 45]. Otherwise, crack and porous structures may form after material mixing and melt pool cooling. Such defects can result from the lack of fusion between layer boundaries,

from thermal stress and interfacial mismatch stresses, and from interfacial bonding between the matrix phase and the reinforcement phase [21, 41, 46]. The study of in-flight melting of single particle aims at giving a better understanding of the whole LENS process.

In this section, a simplified model for the melting of a single particle passing through a laser beam is developed, and an analytical solution is derived. The particle is heated inside of the laser irradiation zone. Several assumptions are made: (1) the top-hat laser has a column shape and uniform intensity throughout the beam; (2) the particle is spherical, and absorbs energy uniformly; (3) the relative velocity between particle and feeding gas is constant inside of the airflow; and (4) particle vaporization is neglected.

The single particle heating equation is generalized by combing the previous models [47-49]. Therefore, the heating and phase change process of a single particle is governed by the following equation:

$$m_p c_{pp} \frac{dT_p}{dt} = \alpha I \frac{S_p}{4} - h S_p (T_p - T_\infty) - \varepsilon \sigma S_p (T_p^4 - T_\infty^4) - \delta L_f \frac{dm_p}{dt} \quad (1a)$$

where

$$\delta = \begin{cases} 0 & T_p \leq T_{sol} \text{ or } T_p \geq T_{liq} \\ 1 & T_{sol} < T_p < T_{liq} \end{cases} \quad (1b)$$

and  $m_p$ ,  $c_{pp}$ , and  $S_p$  are the mass, specific heat, and surface area of a particle;  $T_p$  and  $T_\infty$  are the temperatures of the particle and the surrounding respectively;  $I$  is the laser intensity ( $\text{W}/\text{m}^2$ ), and  $\alpha$  is the laser absorptivity of the particle;  $\varepsilon$  is the surface emissivity of the powder, which equals to 0.19 according to the table of total emissivity;  $\sigma$  is the Stefan-Boltzmann constant ( $5.67 \times 10^{-8} \text{ W}/(\text{m}^2 \cdot \text{K}^4)$ );  $L_f$  is the latent heat of fusion of the particle materials;  $T_{sol}$  and  $T_{liq}$  are solidus and liquidus temperatures of the particle material respectively;  $h$  is the convective heat transfer coefficient, which can be determined from the Nusselt number (Nu) [50]:

$$h = \frac{\text{Nu} k_g}{d_p} = \frac{k_g (2 + 0.6 \text{Re}^{1/2} \text{Pr}^{1/3})}{d_p} \quad (2)$$

where  $d_p$  is the particle diameter;  $k_g$  is the thermal conductivity of the surrounding feeding gas;

$\text{Re} = \frac{\rho_g d_p |v_g - v_p|}{\mu_g}$  is the Reynolds number, where  $\rho_g$ ,  $v_g$ ,  $v_p$ , and  $\mu_g$  are the density of feeding gas, velocity of feeding gas, velocity of the particle, and dynamic viscosity of feeding gas;

$\text{Pr} = \frac{\mu_g c_{pg}}{k_g}$  is the Prandtl number, where  $c_{pg}$  is the specific heat of feeding gas. It should be

noted here that for pure material, there is no solidus and liquidus temperatures. Instead, the material has a single melting point  $T_m$ .

During the particle melting, the latent heat of fusion occurs at melting temperature  $T_m$  (for pure substance), or in a temperature range between  $T_{sol}$  and  $T_{liq}$  (for mixture) [51]. For a number of materials (e.g. Inconel, aluminum oxide), the radiation component is negligible. Therefore, we

restrict our analysis to purely convective heat transfer (i.e. the third term on right side of equation (1) is much smaller than the second term). Under these assumptions, Eq (1) simplifies to:

$$m_p c_{pp} \frac{dT_p}{dt} = \alpha I \frac{S_p}{4} - hS_p (T_p - T_\infty) - \delta L_f \frac{dm_l}{dt} \quad (3a)$$

where

$$m_l = \begin{cases} 0 & T_p \leq T_{sol} \\ \frac{T_p - T_{sol}}{T_{liq} - T_{sol}} m_p & T_{sol} < T_p < T_{liq} \\ m_p & T_p \geq T_{liq} \end{cases} \quad (3b)$$

and  $m_l$  is the mass of the liquid fraction of a particle. Combining equation (3a) with (3b) yields:

$$\left( m_p c_{pp} + \frac{\delta m_p L_f}{T_{liq} - T_{sol}} \right) \frac{dT_p}{dt} = \alpha I \frac{S_p}{4} - hS_p (T_p - T_\infty) \quad (4)$$

Equation (4) can be rewritten as:

$$\frac{d(T_p - A)}{dt} = -B(T_p - A) \quad (5a)$$

where

$$\begin{cases} A = T_\infty + \frac{\alpha I}{4h} \\ B = \frac{hS_p}{m_p c_{pp} + \frac{\delta m_p L_f}{T_{liq} - T_{sol}}} \end{cases} \quad (5b)$$

Solve equation (5) and integrating from an arbitrary time  $t$  to  $t_{sol}$ , which is the time when the particle reaches its solidus temperature, gives:

$$t_{sol} = t - \frac{1}{B_1} \ln \left( \frac{T_{sol} - A}{T_p(t) - A} \right) \quad (6a)$$

where

$$B_1 = \frac{hS_p}{m_p c_{pp}} \quad (6b)$$

The initial temperature of the particle is considered to be the same as that of the surrounding temperature:

$$T_p(t) \Big|_{t=0} = T_\infty \quad (7)$$

Solution of equation (6) gives the time it takes for the particle temperature to rise from room temperature to solidus temperature:

$$t_{sol} = -\frac{1}{B_1} \ln\left(\frac{T_{sol} - A}{T_\infty - A}\right) \quad (8)$$

Similarly, solving equation (5) from  $t_{sol}$  to  $t_{liq}$  yields:

$$t_{sol-liq} = t - \frac{1}{B_2} \ln\left(\frac{T_{liq} - A}{T_p(t) - A}\right) \quad (9a)$$

where

$$B_2 = \frac{hS_p}{m_p c_{pp} + \frac{m_p L_f}{T_{liq} - T_{sol}}} \quad (9b)$$

with the initial condition:

$$T_p(t) \Big|_{t=0} = T_{sol} \quad (10)$$

Solution of equation (9) provides the time needed for the particle temperature to rise from solidus to liquidus temperature:

$$t_{sol-liq} = -\frac{1}{B_2} \ln\left(\frac{T_{liq} - A}{T_{sol} - A}\right) \quad (11)$$

Summing equation (8) and (11) gives the time it takes for the particle to completely melt:

$$t_{melt} = t_{sol} + t_{sol-liq} = -\frac{1}{B_1} \ln\left(\frac{T_{sol} - A}{T_\infty - A}\right) - \frac{1}{B_2} \ln\left(\frac{T_{liq} - A}{T_{sol} - A}\right) \quad (12)$$

For pure substance, there is no second term, and  $T_{sol}$  becomes  $T_m$ . In order for the in-flight melting of a particle to occur, the heating time should be sufficient long for a particle to melt during its flight:

$$t \geq t_{melt} \quad (13)$$

### **3.2 Laser attenuation due to multiple particles**

The study of single particle in-flight melting gives a better understanding of the heating and thus phase change of a particle inside of the laser beam. In the real practice, the laser would pass through multiple particles, and the attenuated laser would heat the substrate to initiate the melt pool. The heated particles then are injected into the melt pool and mix with each other as well as with the substrate material. In this section, the level of energy attenuation due to the particle cloud shadowing effect is studied based on a 2-dimensional (2D) model. We assume that (1) the divergence angle of the particle jet is negligible, i.e. the particle jet is a perfect cylindrical shape; (2) particles are evenly distributed inside each particle jet; (3) particle velocity is constant; and (4) particles collisions are negligible.

According to the Beer-Lambert Law, the attenuated laser intensity  $I$  is given by the following equation:

$$I = I_0 e^{-\mu z} = I_0 e^{-\varepsilon C(z)z} \quad (14)$$

where  $I_0$  is the initial laser intensity,  $\mu$  is the absorption coefficient ( $\text{m}^{-1}$ ),  $C$  (a function of the vertical penetration distance  $z$ ) is the concentration of the particles compound ( $\text{kg}/\text{m}^3$ ), and  $\varepsilon$  is the molecular absorptivity or extinction coefficient ( $\text{m}^2/\text{kg}$ ). The latter can be expressed as [52, 53]:

$$\varepsilon = \frac{E \cdot (1 - \alpha)}{m_p} \quad (15)$$

where  $E$  is half of the surface area of a particle. For a spherical particle  $E = 2\pi r_p^2$ ,  $m = 4\pi r_p^3/3$ , and  $\varepsilon$  can be expressed as follows:

$$\varepsilon = \frac{3(1 - \alpha)}{2r_p \rho_p} \quad (16)$$

The 2D schematic in figure 2 shows a general case of the LENS apparatus with two nozzles. The laser beam has a diameter  $d$ . In order to have a better mixing of the two building materials, the contact widths  $d'$  of both particle jets should be completely overlapping. In addition, the contact width  $d'$  and laser spot diameter  $d$  have the same axis of symmetry. Noted that both the injection angles ( $\theta$ ) and the particle velocities ( $v$ ) can be different for the two materials. Consequently, the nozzles would have different diameters ( $w_1$  and  $w_2$ ).

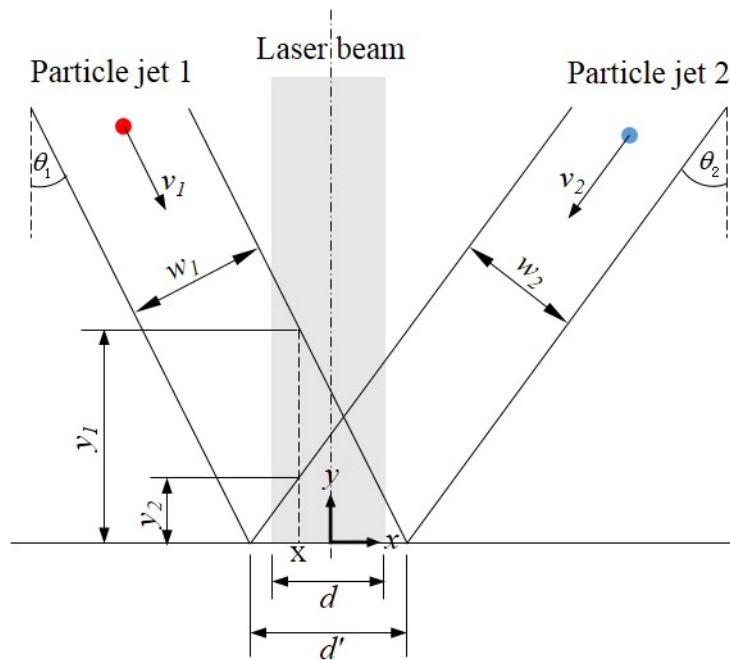


**Figure 2.** 2D schematic of the modified LENS process.

The laser attenuation varies across the beam diameter since the laser beam would pass through different concentrations of particle clouds at different  $x$  positions (see figure 2). The superposition method is applied to solve for the laser attenuation along any vertical pass. For example, at position  $x$  in figure 2, a slice of laser beam passes a layer of particle jet 1 of thickness  $y_1$  and a layer of particle jet 2 of thickness  $y_2$ . Geometrical analysis gives the expressions for  $y_1$  and  $y_2$  respectively:

$$y_1 = -x \cot \theta_1 + \frac{d'}{2} \cot \theta_1 \quad (17)$$

$$y_2 = x \cot \theta_2 + \frac{d'}{2} \cot \theta_2 \quad (18)$$

The laser attenuation at any  $x \in \left[-\frac{d}{2}, \frac{d}{2}\right]$  can then be obtained from equation (14):

$$I = I_0 \exp \left[ -\varepsilon \frac{M_{p1}}{\pi \left(\frac{w_1}{2}\right)^2 V_1} y_1 \right] \cdot \exp \left[ -\varepsilon \frac{M_{p2}}{\pi \left(\frac{w_2}{2}\right)^2 V_2} y_2 \right] \quad (19)$$

where  $M_{p1}$  and  $M_{p2}$  are the feeding rates of the two materials respectively.

It can be seen that the shadowing effect is functions of particle properties, particle feeding rates, particle velocities, nozzle sizes and injection angles. The laser intensity and powder feeding parameters can be modified to fabricate different types of heterogeneous objects. Consequently, the shadowing effect would be varied.

### **3.3 Substrate heating temperature distribution**

In this study, alumina ceramic and Inconel 718 powders are taken as an example to fabricate cermet composite. Cermet composite, which consists of ceramic phase and metal phase, has superior engineering performance, such as high strength and hardness, high temperature resistance and corrosion resistance, chemical stability, and ability to undergo plastic deformation. The building materials are Inconel 718 and alumina ceramic powders, and the substrate material is Inconel 718. Inconel 718, an oxidation and corrosion resistant nickel based alloy, has a good weldability and high temperature application. Argon is used as feeding gas that provides an oxygen-free environment.

The major component of alumina ceramic is aluminum oxide  $\text{Al}_2\text{O}_3$  (>90%) and silicon dioxide  $\text{SiO}_2$  (<10%). The properties of alumina ceramic depend on the properties of the two major components. Both the specific heat and the thermal conductivity of Inconel 718 can be approximated by a piecewise polynomial function of temperature [54, 55]. For the sake of simplicity and without loss of generality, in this study we assume that both the specific heat and the thermal conductivity of Inconel 718 be constant and equal to 600 J/(kg·K) and 21.3 W/(m·K), respectively [56, 57]. The laser absorptivity here is assumed constant and equal to 0.3 [47]. The physical properties used are listed in table 1.

The incident energy on the substrate is composed of two parts: the energy carried by the heated particles and the transmitted laser energy [52]. Since the substrate should be melt before contacting the liquid or solid particles to form a firm bonding, we do not consider the energy carried by the particles. Only the attenuated laser energy is considered as the incident heat source onto the substrate.

**Table 1.** Physical properties of building material components [57, 58]

	Inconel 718	Al <sub>2</sub> O <sub>3</sub>	SiO <sub>2</sub>
Laser absorptivity, $\alpha$	0.3	0.3	0.3
Density, $\rho$ (kg/m <sup>3</sup> )	8190	3950	2650
Specific heat, $c_{pp}$ (J/kg/K)	600	880	730
Thermal conductivity, $k_p$ (W/m/K)	21.3	30	1.5
Latent heat of fusion, $L_f$ (kJ/kg)	272	1067	237
Melting point, $T_m$ (K)	$T_{sol} = 1533$ $T_{liq} = 1609$	2345	1998

Figure 3 shows a 2D schematic for the substrate heating model. The calculation is performed on a 3 mm × 3 mm rectangular domain. The laser beam is moving over the substrate, with its left edge moving from  $x = 0$  to  $x = 1.5$  mm. The model is based on the following assumptions: (1) convective heat transfer coefficient is at constant 100 W/(m<sup>2</sup>·K); (2) convection within the melt pool is negligible.

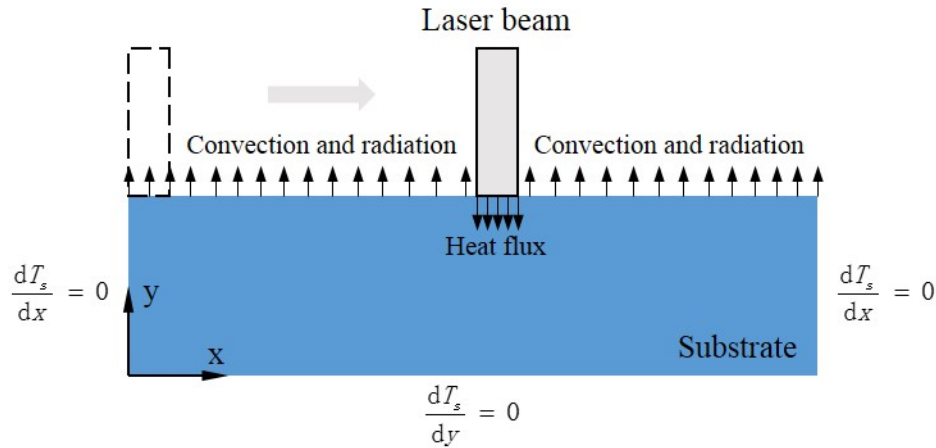


**Figure 3.** 2D Schematic for the substrate heating model.

The temperature distribution of the heated substrate is based on the following 2D heat conduction governing equation [42, 47]:

$$\rho_s c_{ps} \frac{dT_s}{dt} = \frac{\partial}{\partial x} \left( k_s \frac{\partial T_s}{\partial x} \right) + \frac{\partial}{\partial y} \left( k_s \frac{\partial T_s}{\partial y} \right) + S \quad (20)$$

where  $\rho_s$ ,  $c_{ps}$ , and  $k_s$  are the density, specific heat, and thermal conductivity of substrate material;  $T_s$  is the substrate temperature;  $S$  is the volume heat source (W/m<sup>3</sup>) generated on surface of the substrate:

$$S = \alpha I \mu e^{-\mu y} \quad (21)$$

Solution of equation (20) provides the temperature profile inside of the substrate when exposed to a uniform surface heat source of intensity  $\alpha I$  distributed as  $exp(-\mu y)$  with depth. For metals, at optical wavelength below 400 nm, the absorption coefficient  $\mu$  is typically  $10^6$  (cm<sup>-1</sup>) [42, 59].

The initial temperature in the calculation domain is the room temperature, which is set to 298 K. The upper edge of the calculation domain beneath the laser spot is subject to the following heat flux boundary condition:

$$-k_s \frac{dT_s}{dy} = -\alpha I \quad (22)$$

The top edge of the calculation domain outside of the laser spot region is subject to a convective-radiative Neumann boundary condition:

$$-k_s \frac{dT_s}{dy} = h(T_s - T_\infty) + \varepsilon \sigma (T_s^4 - T_\infty^4) \quad (23)$$

The remaining three edges of the calculation domain are subject to thermal insulation:

$$-n \left( -k_s \frac{dT_s}{dn} \right) = 0 \quad (24)$$

FTCS (Forward-Time Central-Space) explicit scheme is used to solve equation (20). The time step is based on the Fourier number (Fo), and numerical stability must satisfy the following condition:

$$Fo = \frac{k_s \Delta t}{\rho_s c_{ps} \min(\Delta x, \Delta y)^2} \leq 0.25 \quad (25)$$

where  $\Delta t$  is time step;  $\Delta x$  and  $\Delta y$  are the unit cell lengths in  $x$  and  $y$  directions. The computational domain is divided into  $400 \times 120$  cells of uniform size  $\Delta x = \Delta y = 2.5 \times 10^{-5}$  m. The Fourier number is set to 0.15, and the corresponding time step is  $2.23 \times 10^{-5}$  s.

Figure 4 shows the temperature distribution at a fixed instance in time ( $t=0.5$ s) generated by a moving laser for two different powers, i.e. 75 W (Figure 4(a)) and 150 W (Figure 4(b)). The lower boundary of the melt pool shape is considered as the isothermal surface at the melting point [60]. Figure 4 shows that the melt pool width (along  $x$ -axis) can be either narrower or wider than the actual laser spot size. Therefore, the powder nozzle size should be carefully select to be fit to the melt pool size for optimization step.

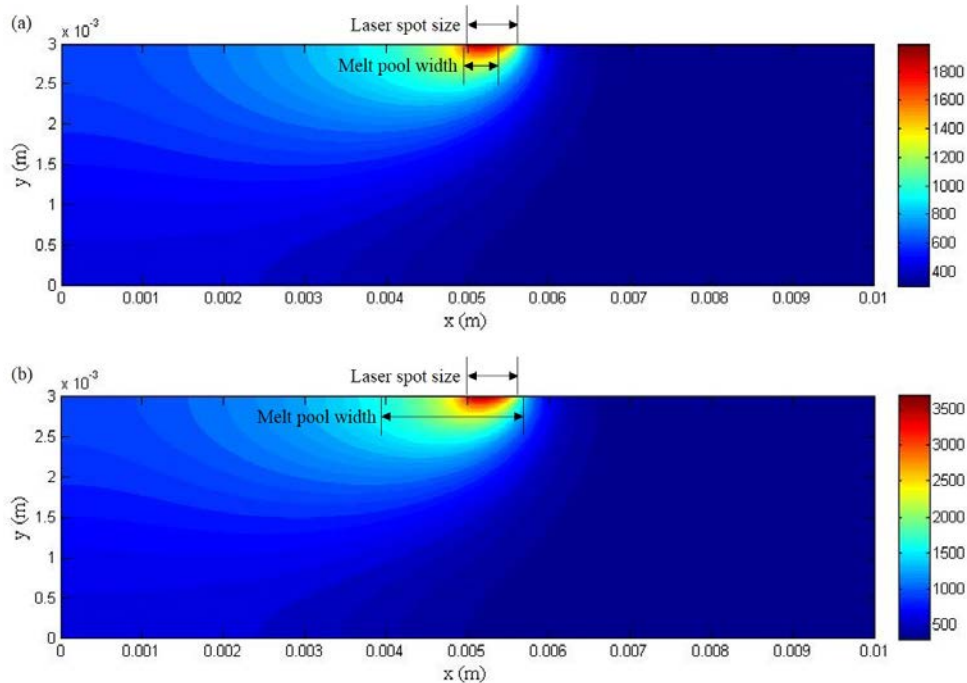


**Figure 4.** Substrate temperature distribution when laser moves from left side to the center of the calculation domain, without considering powder injection: (a) laser power 75 W, and (b) laser power 150 W.

#### **4. Optimization of the process parameters**

Theoretical models for the inflight melting, laser attenuation, and substrate heating have been developed in the previous sections. In order to optimize the whole process, two sets of parameters need to be considered in general: laser parameters and powder parameters. The objective is to determine the optimized process parameters so as to guarantee as much concurrent in-flight melting of different particles while melting the substrate.

Although solid-particle/liquid-substrate can form a good cladding, the repelling force between solid-particle and liquid-substrate is larger, thus a possible lower deposition efficiency is obtained [25, 61]. Therefore, liquid-particle/liquid-substrate is preferred. In the real case, a certain amount of particles do not have sufficient interaction with the laser beam during their flight, and may still be solid state when in contact with the substrate, as can be seen in figure 1. However, it has been demonstrated that a spherical particle melts instantly inside of the pool with constant melting temperature: A 10- $\mu\text{m}$ -diameter particle would completely melt in the order of  $10^{-5}$  second, and a 100- $\mu\text{m}$ -diameter particle would completely melt in the order of  $10^{-4}$  second [62, 63]. So even particles are not melt during the flight, they should be deposited on a melt pool position with the temperature higher than their melting points.

Figure 4 shows that the melt pool temperature gradients are higher ahead of the laser (e.g. to the right side of the laser spot when the laser is moving from left to right). This suggests that particles with higher melting point should be injected behind the moving laser. The space behind the moving laser spot provides the instant contact melting of the non-in-flight-melted ceramic,

which has a higher melting point than Inconel. Hence ceramic powders are placed in the feeder on the left side while Inconel 718 powders are placed in the feeder on the right side.

The process parameter values are those of the OPTOMECH MR-7 and are listed in table 2. A 500 W laser is chosen for optimization, and the laser power can be varied from 12% to full power. Though the laser spot size and laser moving velocity are a priori adjustable, they are set to typically used values. The particle/injection velocity is constant and we assume that the feed rate and/or particle concentration does not affect the particle/injection velocity. The powder feeding rate and the particle radius are those specified by the machine manufacturers. The injection angle and nozzle diameter are generally adjustable parameters.

**Table 2.** Value range of process parameters

Parameter	Value
Laser parameters	
Laser power, $P_l$ (W)	60-500
Laser spot radius, $r_l$ ( $\mu\text{m}$ )	300
Laser moving velocity, $v_l$ (mm/s)	10
Powder parameters	
Injection angle, $\theta_i$ ( $^\circ$ )	15-75
Injection velocity, $v_i$ (m/s)	0.5-20
Feeding rate, $M_{pi}$ (g/min)	0.5-10
Particle radius, $r_{pi}$ ( $\mu\text{m}$ )	10
Nozzle diameter, $w_i$ (mm)	0.5-3

The system under study is characterized by a number of coupled physical process and process parameters, which can span a wide range of values. In particular, the incident laser intensity is attenuated by particle clouds and is dependent on powder parameters. In turn, the melt pool size, which depends on the attenuated laser intensity, plays an important role in determining the powder parameters (such as injection angle and nozzle diameter). Finally, the result of all these parameters would determine the laser attenuation level. To account for the coupling between different processes, we propose an iterative optimization procedure, whose schematic flowchart is shown in figure 5. We demonstrate its applicability with a test case.

The starting point (Block 1 in figure 5) is a selected laser intensity  $I$ , which is assumed to be the “attenuated” laser intensity. To reversely obtain a proper initial laser intensity, three modules are applied: particles in-flight melting, laser attenuation, and laser intensity validation.

For the particles in-flight melting module, the temperature distribution is first generated based on the laser intensity  $I$  and the given laser moving velocity  $v_l$ . The maximum temperature on the substrate should be lower than the boiling point of Inconel 718. Otherwise, we adjust the laser intensity to a lower level. In the example, the laser power chosen is 125 W, resulting in a laser intensity of  $4.42 \times 10^8 \text{ W/m}^2$ . Condition 1 (Block 1 in figure 5) is used to determine the particle jet boundary, or the contact width  $d'$  between a particle jet and the substrate. Illustrated

in figure 6, the left and right boundaries of  $d'$  are determined by the melting points of alumina ceramic and Inconel 718 respectively, and the critical distances  $d_1$  and  $d_2$  are the distances from the left and right boundaries to the center line of laser beam respectively. Then to guarantee the instant melting of the particles inside of the melt pool, the contact width  $d'$  is determined by:

$$d' = 2 \min\{d_1, d_2\} \quad (26)$$

The calculation grid resolution is  $25 \mu\text{m}$ , which is close to the smallest particle diameter. The two critical distances are calculated as:  $d_1=d_2=0.35 \text{ mm}$ , so the contact width  $d'=0.7 \text{ mm}$ .

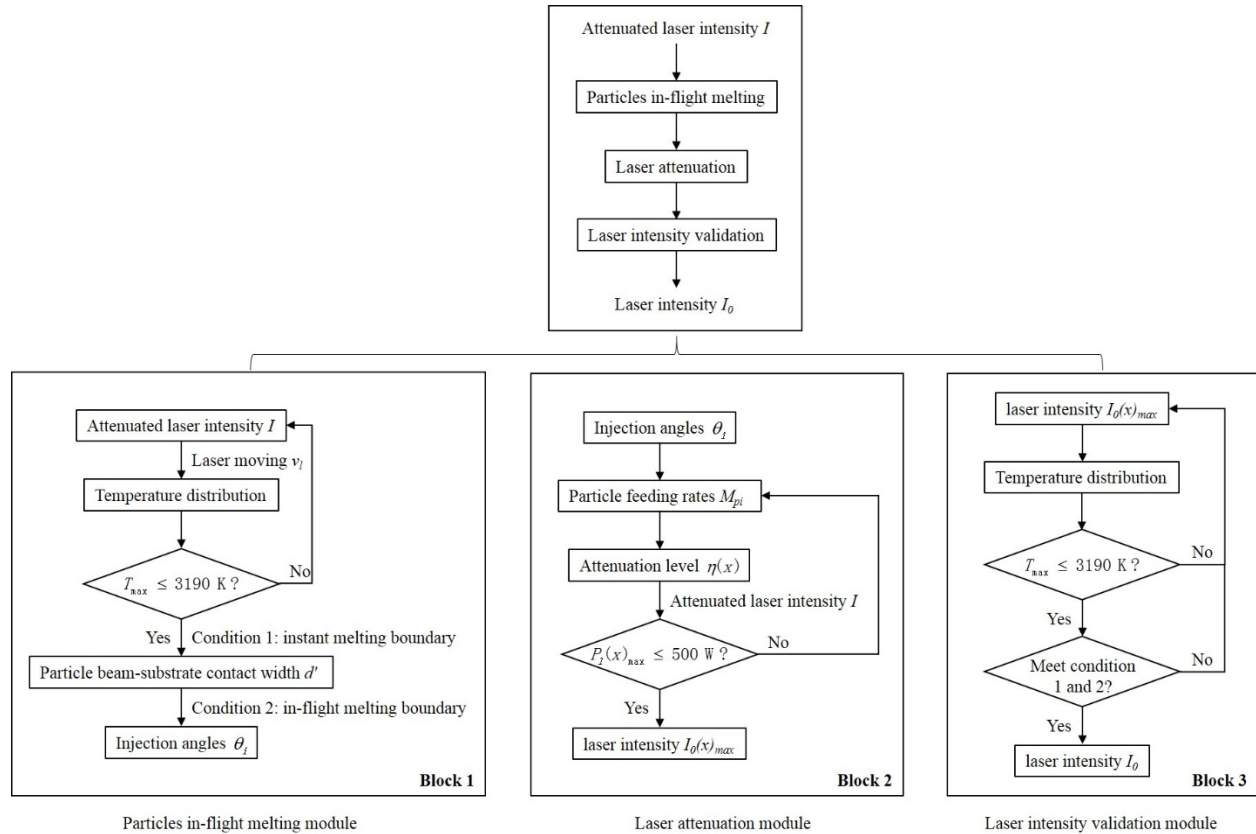


**Figure 5.** Process parameters optimization flowchart.

Condition 2 (Block 1 in figure 5) is to ensure the melting of the particles, i.e. the particles should be either in-flight melted or instantly melted when in contact with the substrate. It can be seen from figures 6 and 7 that substrate surface temperature on the left side of point P (within  $d'$ ) is above 2345 K, which is high enough to guarantee the melting of ceramic particles. On the right side of point P, the substrate surface temperature is below the melting point of ceramic, thus in-flight melting plays an important role herein. It can be seen in figure 7, trajectory 1 (marked as Traj 1) is shorter than any trajectory above it. Therefore, for ceramic, the condition 2 would be fulfilled if a particle going along trajectory 1 is able to melt during its flight. For Inconel 718, even particles traveling through the longest trajectory (Traj 2) are not able to melt during the flight, condition 2 is still fulfilled. That is because the substrate surface temperature within  $d'$  is above the melting point of Inconel 718, and can guarantee the instant melting of Inconel particles when in contact with the substrate.

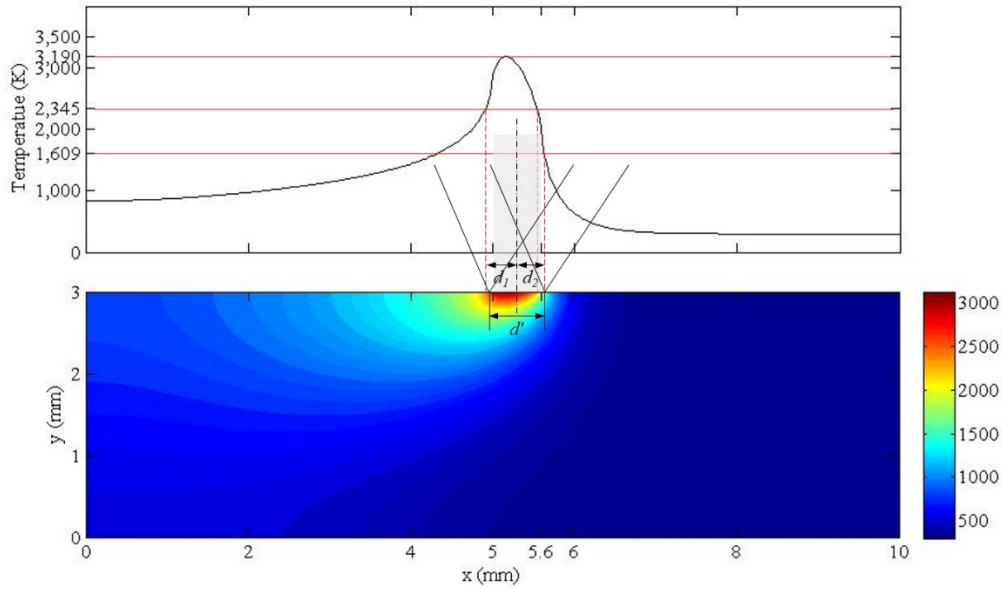


**Figure 6.** Schematic for condition 1: instant melting boundary.

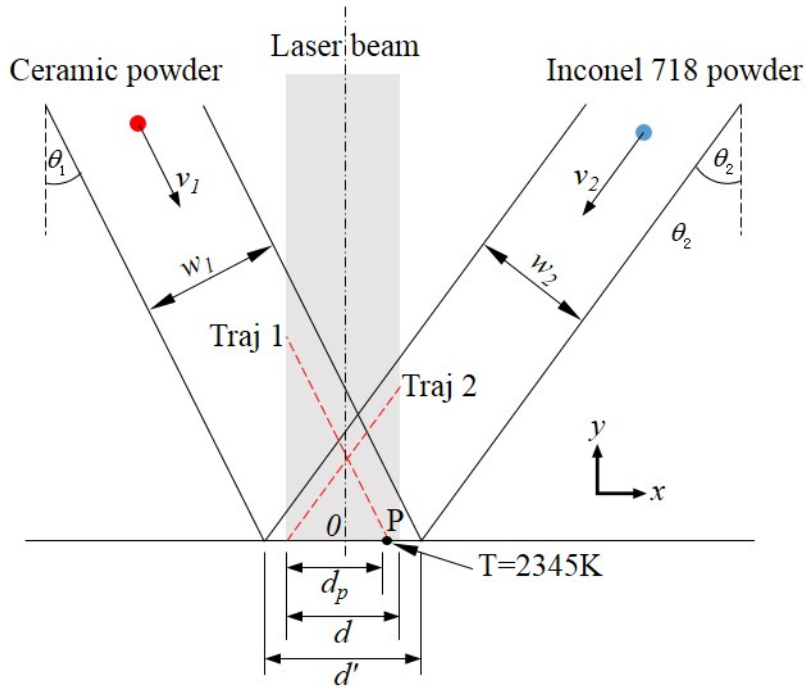


**Figure 7.** Schematic for conditions 2: in-flight melting boundary.

To solve for the injection angles, the following constraints are applied by combining equations (12) and (13):

$$\frac{d_p}{v_1 \sin \theta_1} \geq t_{melt} = 1.548 \times 10^{-3} \text{ s} \quad (27)$$

The calculated value range of injection angle is:  $\theta_1 \leq 20^\circ$ , providing the particle velocities are 1 m/s and particle radius is 20  $\mu\text{m}$ . There is no specific limitation for  $\theta_2$ . For simplicity and symmetry (although not necessary), choose  $\theta_2 = \theta_1 = 20^\circ$ , then

$$w_1 = w_2 = d' \cos \theta \approx 0.7 \text{ mm} \quad (28)$$

For the laser attenuation module (Block 2 in figure 5), equation (19) is used to determine the laser attenuation, given particle velocities, injection angles  $\theta_i$  and powder feeding rates  $M_{pi}$ . If ceramic and Inconel 718 are mixed with any fixed proportion, i.e.  $M_{p2} = n \cdot M_{p1}$  ( $n$  is a real number), then equation (19) becomes:

$$I = I_0 \exp \left[ - \frac{12(1 - \alpha) \left( \frac{d'}{2} - x \right) M_{p1}}{\pi r_p \rho_{p1} d'^2 v \sin(2\theta)} - \frac{12(1 - \alpha) \left( \frac{d'}{2} + x \right) M_{p2}}{\pi r_p \rho_{p2} d'^2 v \sin(2\theta)} \right] \quad (29)$$

In order to obtain the maximum value of initial laser intensity  $I_0(x)_{max}$ , one has to minimize the term in the bracket of equation (29), or to maximize the object function:

$$\text{object function} = \frac{12(1 - \alpha) \left( \frac{d'}{2} - x \right) M_{p1}}{\pi r_p \rho_{p1} d'^2 v \sin(2\theta)} + \frac{12(1 - \alpha) \left( \frac{d'}{2} + x \right) M_{p2}}{\pi r_p \rho_{p2} d'^2 v \sin(2\theta)} \quad (30)$$

The solution is:

$$\begin{cases} x = \frac{d}{2} & \text{if } \frac{M_{p2}}{\rho_{p2}} - \frac{M_{p1}}{\rho_{p1}} > 0 \\ x = -\frac{d}{2} & \text{if } \frac{M_{p2}}{\rho_{p2}} - \frac{M_{p1}}{\rho_{p1}} < 0 \end{cases} \quad (31)$$

If, e.g. ceramic and Inconel 718 are mixed with equal proportion, i.e.  $M_{p1} = M_{p2}$ , then the object function is maximum at  $x = -\frac{d}{2}$ . From equation (29), the attenuation level at  $x = -\frac{d}{2}$  is 30% given  $M_{p1} = M_{p2} = 0.5 \text{ g/min}$ . Then the maximum value of initial laser intensity  $I_0(x)_{max}$  can be calculated accordingly. The maximum initial laser power is 417 W.

The last module is the laser intensity validation. The substrate temperature distribution should be regenerated with the new laser intensity as well as considering the laser attenuation. The highest temperature on the substrate should be no higher than the boiling point of the substrate material. Then validate the temperature at the two boundaries of  $d'$ : the left and right boundary temperatures should be no lower than 2345 K and 1609 K respectively.

If any of these constraints is not met, then a decrease of the initial laser power is required. The bisection method is used to determine the optimum initial laser power between 125 W and

417 W until the difference between two adjacent runs is smaller than 1 W. This procedure yields an optimum laser power of 320 W.

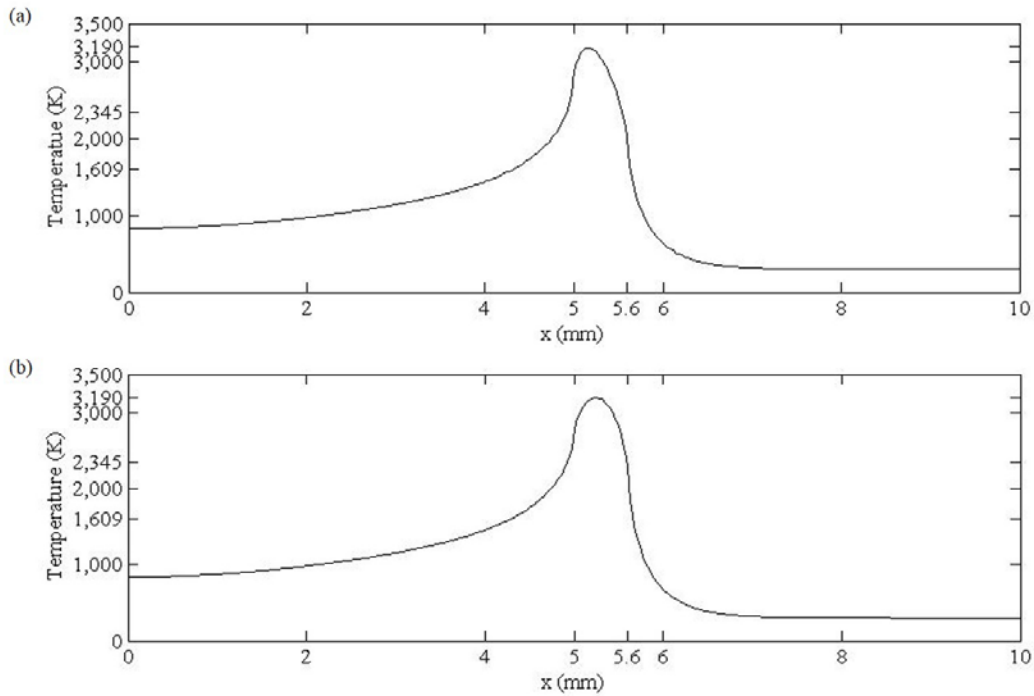


**Figure 8.** Substrate surface temperature comparison: (a) 125 W laser without powder injection, and (b) 320 W laser with powder injection.

## **5. Discussion and conclusions**

The substrate surface temperature profiles before and after the addition of powders are plotted in figure 8 (a) and (b) respectively. Both profiles show that the surface temperature decreases faster in front of the beam travelling direction than behind the beam. It should be noted that the peak of the temperature valley rests near the rear of the laser spot instead of in the middle, but the peak temperature turns to be in the middle of the laser spot as particles are injected in figure 8 (b). Moreover, the temperature profile is more “symmetric” if particles are injected. This is because the ceramic powders are injected from the left while the Inconel powders are injected from the right, and the shadowing effect is more obvious at the left given the same feeding rates for both materials. This is, actually, an advantage that might be considered in future optimization, since a “symmetric” temperature profile would result in a more uniform material fusion and a higher manufacturing accuracy.

The briefly introduced parameter optimization process is just an example of using a starting laser powder of 125 W. However, the parameter selection can be within a given range. In the example, the results are based on 20° injection angles, which can be modified still. In order to increase the injection angles, a larger laser spot size or a larger laser moving velocity would be needed. The starting laser intensity, the laser moving velocity, the injection angles as well as other parameters should be carefully selected to meet the optimization constraints described in the flowchart.

In this study, a material in-flight melting (including instant melting at melt pool) model for the modified multi-material LENS process has been developed. The model includes the single particle in-flight melting, which investigates the thermal behavior of the particle flow, the particle clouds shadowing effect on the laser intensity, and the heating and melt pool formation of the substrate. A reversed optimization method is developed and the corresponding flowchart is used to optimize the various process parameters. The in-flight melting as well as instant melting at the melt pool conditions are applied to determine the boundaries of process parameters.

The result of the cermet composite material fabrication example in the study shows that with a 320 W, 600  $\mu\text{m}$  spot diameter laser moving at 10 mm/s, the optimized powder parameters are: 20° injection angles, 1 m/s injection velocities, 0.5 g/min material feeding rate, 20  $\mu\text{m}$  particle diameter, and 0.7 mm nozzle diameters. Moreover, the Inconel 718 powders should be injected in the front of the laser moving direction, while the ceramic powders be injected from the rear.

This study is a first step towards the optimization and fabrication of heterogeneous components using LENS technique. The model provides helpful information to the optimization of real LENS applications. The development of operating diagrams to facilitate the optimization process is subject to current research. Also, generalizations to fully 3D simulations, the full cladding layer development process (which includes the cooling, second-layer effect, and quality prediction), economic aspects and fabrication efficiency (e.g. energy costs) and component quality will be subject of future research. Finally, experimental validation and comparison would be needed in the future to substantiate any proposed model.

### References

- [1] Kou, X.Y., and Tan, S.T., 2007, "Heterogeneous Object Modeling: a Review," *Computer-Aided Design*, Vol. **39**(4), pp. 284-301.
- [2] Torquato, S., 2010, "Optimal Design of Heterogeneous Materials," *Annual Review of Materials Research*, Vol. **40**(1), pp. 101-129.
- [3] Zhou, H., Liu, J., and Lu, B., 2009, "Heterogeneous Object Modeling Based on Multi-Color Distance Field," *Materials and Design*, Vol. **30**(4), pp. 939-946.
- [4] Koizumi, M., 1997, "FGM Activities in Japan," *Composites Part B: Engineering*, Vol. **28**(1-2), pp. 1-4.
- [5] Wosko, M., Paszkiewicz, B., Piasecki, T., Szyszka, A., Paszkiewicz, R., and Tlaczala, M., 2005, "Applications of Functionally Graded Materials in Optoelectronic Devices," *Optica Applicata*, Vol. **35**(3), pp. 663-667.
- [6] Pompe, W., Worch, H., Epple, M., Friess, W., Gelinsky, M., Greil, P., Hempel, U., Scharnweber, D., and Schulte, K., 2003, "Functionally Graded Materials for Biomedical Applications," *Materials Science and Engineering: A*, Vol. **362**(1-2), pp. 40-60.
- [7] Bandyopadhyay, A., Krishna, B.V., Xue, W., and Bose, S., 2009, "Application of Laser Engineered Net Shaping (LENS) to Manufacture Porous and Functionally Graded Structures for Load Bearing Implants," *Journal of Materials Science*, Vol. **44**(20), pp. S29-S34.
- [8] Huang, J., and Fadel, G., 2000, "Heterogeneous Flywheel Modeling and Optimization," *Materials and Design*, Vol. **21**(2), pp. 111-125.

- [9] Morvan, S., 2001, "MMa-Rep, a Representation for Multimaterial Solids," *Ph. D. thesis*, Clemson University.
- [10] Huang, J., and Fadel, G., 2001, "Bi-Objective Optimization Design of Heterogeneous Injection Mold Cooling Systems," *Journal of Mechanical Design*, Vol. **123**(2), pp. 226-239.
- [11] Qian, X., and Dutta, D., 2003, "Design of Heterogeneous Turbine Blade," *Computer-Aided Design*, Vol. **35**(3), pp. 319-329.
- [12] Xing, A., Zhao, J., Huang, C., and Zhang, J., 1998, "Development of an Advanced Ceramic Tool Material-Functionally Gradient Cutting Ceramics," *Materials Science and Engineering*, Vol. **A248**, pp. 125-131.
- [13] Kong, C.Y., and Soar, R.C., 2005, "Fabrication of Metal-Matrix Composites and Adaptive Composites Using Ultrasonic Consolidation Process," *Materials Science and Engineering A*, Vol. **412**(1-2), pp. 12-18.
- [14] Ran, G., Robinson, C., Yang, Y., and Stucker, B., 2007, "Use of Ultrasonic Consolidation for Fabrication of Multi-Material Structures," *Rapid Prototyping Journal*, Vol. **13**(4), pp. 226-235.
- [15] Fessler, J., Nickel, A., Link, G., and Prinz, F., 1997, "Functional Gradient Metallic Prototypes through Shape Deposition Manufacturing," *Proceedings of Symposium on Solid Freeform Fabrication*, University of Texas at Austin, Austin, Texas.
- [16] Binnard, M., 1999, "Design by Composition for Rapid Prototyping," *Ph. D. thesis*, Stanford University.
- [17] Agarwala, M., Bourell, D., Beaman, J., Marcus, H., and Barlow, J., 1995, "Direct Selective Laser Sintering of Metals," *Rapid Prototyping Journal*, Vol. **1**(1), pp. 26-36.
- [18] Kruth, J-P., Mercelis, P., Vaerenbergh, J.V., Froyen, L., and Rombouts, M., 2005, "Binding Mechanisms in Selective Laser Sintering and Selective Laser Melting," *Rapid Prototyping Journal*, Vol. **11**(1), pp. 26-36.
- [19] Khor, K.A., and Gu, Y.W., 2000, "Thermal Properties of Plasma-Sprayed Functionally Graded Thermal Barrier Coatings," *Solid Thin Films*, Vol. **372**(1-2), pp. 104-113.
- [20] Kieback, B., Neubrand, A., and Riedel, H., 2003, "Processing Techniques for Functionally Graded Materials," *Materials Science and Engineering A*, Vol. **362**(1-2), pp. 81-105.
- [21] Liu, W., and DuPont, J.N., 2003, "Fabrication of Functionally Graded TiC/Ti Composites by Laser Engineered Net Shaping," *Scripta Materialia*, Vol. **48**(9), pp. 1337-1342.
- [22] Kumar, S., and Kruth, J.P., 2010, "Composites by Rapid Prototyping Technology," *Materials and Design*, Vol. **31**(2), pp. 850-856.
- [23] Sun, S., Durandet, Y., and Brandt, M., 2004, "Parametric Investigation of Pulsed Nd: YAG Laser Cladding of Stellite 6 on Stainless Steel," *Surface and Coatings Technology*, Vol. **194**(2-3), pp. 225-231.
- [24] Toyserkani, E., Khajepour, A., and Corbin, S., 2004, "3-D Finite Element Modeling of Laser Cladding by Powder Injection: Effects of Laser Pulse Shaping on the Process," *Optics and Lasers in Engineering*, Vol. **41**(6), pp. 849-867.
- [25] Oliveira, U., Ocelík, V., and Hosson, J.Th.M., 2005, "Analysis of Coaxial Laser Cladding Processing Conditions," *Surface and Coatings Technology*, Vol. **197**(2-3), pp. 127-136.
- [26] Yakovlev, A., Trunova, E., Grevey, D., Pilloz, M., and Smurov, I., 2005, "Laser-Assisted Direct Manufacturing of Functionally Graded 3D Objects," *Surface and Coatings Technology*, Vol. **190**(1), pp. 15-24.

- [27] Zhu, G., Li, D., Zhang, A., and Tang, Y., 2011, "Numerical Simulation of Metallic Powder Flow in a Coaxial Nozzle in Laser Direct Metal Deposition," *Optics and Laser Technology*, Vol. **43**(1), pp. 106-113.
- [28] Milewski, J., Lewis, G., Thoma, D., Keel, G., Nemeč, R., and Reinert, R., 1998, "Directed Light Fabrication of a Solid Metal Hemisphere Using 5-Axis Powder Deposition," *Journal of Materials processing Technology*, Vol. **75**(1-3), pp. 165-172.
- [29] Majumdar, J., Pinkerton, A., Liu, Z., Manna, I., and Li, L., 2005, "Microstructure Characterisation and Process Optimization of Laser Assisted Rapid Fabrication of 316L Stainless Steel," *Applied Surface Science*, Vol. **247**(1-4), pp. 320-327.
- [30] Krishna, B.V., Bose, Su., and Bandyopadhyay, A., 2008, "Fabrication of Porous NiTi Shape Memory Alloy Structures Using Laser Engineered Net Shaping," *Journal of Biomedical Materials Research Part B: Applied Biomaterials*, Vol. **89**(2), pp. 481-490.
- [31] Espana, F. A., Balla, V. K., Bose, S., and Bandyopadhyay, A., 2010, "Design and Fabrication of CoCrMo Alloy Based Novel Structures for Load Bearing Implant Using Laser Engineered Net Shaping," *Material Science and Engineered C*, Vol. **30**(1), pp. 50-57.
- [32] Paul, C., Ganesh, P., Mishra, S., Bhargava, P., Negi, J., and Nath, A., 2007, "Investigating Laser Rapid Manufacturing for Inconel-625 Components," *Optics and Laser Technology*, Vol. **39**(4), pp. 800-805.
- [33] Savitha, U., Gokhale, H., Reddy, G.J., Venkataramana, A., Gokhale, A.A., and Sundararaman, M., 2012, "Effect of Process Parameters on Porosity in Laser Deposited In625 Alloy," *Transactions of the Indian Institute of Metals*, Vol. **65**(6), pp. 765-770.
- [34] Palčić, I., Balazic, M., Milfelner, M., and Buchmeister, B., 2009, "Potential of Laser Engineered Net Shaping (LENS) Technology," *Materials and Manufacturing Processes*, Vol. **24**(7-8), pp. 750-753.
- [35] Cottam, R., Barry, T., and Brandt, M., 2013, "A Theoretical Processing Map for Laser Cladding: Experimental Validation with Laser Cladding of Ti-6Al-4V Powder on a Ti-6Al-4V Substrate," *Journal of Physical Science and Application*, Vol. **3**(5), pp. 287-294.
- [36] Schwendner, K.I., Banerjee, R., Collins, P.C., Brice, C.A., and Fraser, H.L., 2001, "Direct Laser Deposition of Alloys from Elemental Powder Blends," *Scripta Materialia*, Vol. **45**(10), pp. 1123-1129.
- [37] Collins, P.C., Banerjee, R., and Fraser, H.L., 2003, "The Influence of the Enthalpy of Mixing During the Laser Deposition of Complex Titanium Alloys Using Elemental Blends," *Scripta Materialia*, Vol. **48**(10), pp. 1445-1450.
- [38] Domack, M.S., and Baughman, J.M., 2005, "Development of Nickel-Titanium Graded Composition Components," *Rapid Prototyping Journal*, Vol. **11**(1), pp. 41-51.
- [39] Zhong, M., Liu, W., Zhang, Y., and Zhu, X., 2006, "Formation of WC/Ni Hard Alloy Coating by Laser Cladding of W/C/Ni Pure Element Powder Blend," *International Journal of Refractory Metals and Hard Materials*, Vol. **24**(6), pp. 453-460.
- [40] Shin, K., Natsu, H., Dutta, D., and Mazumder, J., 2003, "A Method for the Design and Fabrication of Heterogeneous Objects," *Materials and Design*, Vol. **24**(5), pp. 339-353.
- [41] Lewis, G. K., and Schlienger, E., 2000, "Practical Considerations and Capabilities for Laser Assisted Direct Metal Deposition," *Materials and Design*, Vol. **21**(4), pp. 417-423.
- [42] Duley, W.W., "UV Lasers: Effects and Applications in Materials Science," Cambridge: University Press, 1996. Print.
- [43] Otto, A., and Schmidt, M., 2010, "Towards a Universal Numerical Simulation Model for Laser Material Processing," *Physics Procedia*, Vol. **5**, pp. 35-46.

- [44] Vásquez, F., Ramos-Grez, J.A., and Walczak, M., 2012, "Multiphysics Simulation of Laser–Material Interaction during Laser Powder Deposition," *International Journal of Advanced Manufacturing Technology*, Vol. **59**(9-12), pp. 1037-1045.
- [45] Schneider, M., 1968, "Laser Cladding with Powder: Effect of Some Machining Parameters on Clad Properties," *Ph.D. thesis*, University of Twente, Enschede, Netherlands.
- [46] Man, H.C., Zhang, S., Cheng, F.T., and Yue, T.M., 2001, "Microstructure and Formation Mechanism of in situ Synthesized TiC/Ti Surface MMC on Ti-6Al-4V by Laser Cladding," *Scripta Materialia*, Vol. **44**(12), pp. 2801-2807.
- [47] Gruzicic, M., Hu, Y., Fadel, G.M., and Keicher, D.M., 2000, "Optimization of the LENS Rapid Fabrication Process for In-Flight Melting of Feed Powder," *Journal of Materials Synthesis and Processing*, Vol. **9**(5), pp. 223-233.
- [48] Liu, C., and Liu, J., 2003, "Thermal Process of a Powder Particle in Coaxial Laser Cladding," *Optics and Laser Technology*, Vol. **35**(2), pp. 81-86.
- [49] Wen, S.Y., Shin, Y.C., Murthy, J.Y., and Sojka, P.E., 2009, "Modeling of Coaxial Powder Flow for the Laser Direct Deposition Process," *International Journal of Heat and Mass Transfer*, Vol. **52**(25-26), pp. 5867-5877.
- [50] Gu, S., McCartney, D.G., Eastwick, C.N., and Simmons, K., 2004, "Numerical Modeling of In-Flight Characteristic of Inconel 625 Particle During High-Velocity Oxy-Fuel Thermal Spraying," *Journal of Thermal Spray Technology*, Vol. **13**(2), pp. 200-213.
- [51] Yu, K., "Modeling for Casting and Solidification Processing," Florida: CRC press, 2001. Print.
- [52] Jouvard, J.M., Grevey, D.F., Lemoine, F., and Vannes, A.B., 1997, "Continuous Wave Nd: YAG Laser Cladding Modeling: a Physical Study of Track Creation during Lower Power Processing," *Journal of Laser Applications*, Vol. **9**(1), pp. 43-50.
- [53] Zhou, J., and Liu, H., "Laser Rapid Manufacturing Technology and Application," Beijing: Chemical Industry Press, 2009. Print.
- [54] Brooks, C.R., Cash, M., and Garcia, A., 1978, "The Heat Capacity of Inconel 718 from 313 to 1053 K," *Journal of Nuclear Materials*, Vol. **78**(2), pp. 419-421.
- [55] Pottlacher, G., Hosaeus, H., Kaschnitz, E., and Seifer, A., 2002, "Thermal Properties of Solid and Liquid Inconel 718 Alloy," *Scandinavian Journal of Metallurgy*, Vol. **31**(3), pp. 161-168.
- [56] Kamnis, S., Gu, S., and Zeoli, N., 2008, "Mathematical Modelling of Inconel 718 Particles in HVOF Thermal Spraying," *Surface and Coating Technology*, Vol. **202**(12), pp. 2715-2724.
- [57] Perry, R.H., Green, D.W., and Maloney, J.O., "Perry's Chemical Engineer's Handbook Seventh Edition," Chicago: R. R. Donnelley & Sons Company Press, 1997. Print.
- [58] Chen, H., Pinkerton, A.J., and Li, L., 2010, "Fiber Laser Welding of Dissimilar Alloys of Ti-6Al-4V and Inconel 718 for Aerospace Applications," *International Journal of Manufacturing Technology*, Vol. **52**(9-12), pp. 977-987.
- [59] Brown, M.S., and Arnold, C.B., 2010, "Fundamentals of Laser-Material Interaction and Application to Multiscale Surface Modification," *Laser Precision Microfabrication*, Vol. **135**, pp. 91-120.
- [60] Fathi, A., Toyserkani, E., Khajepour, A., and Durali, M., 2006, "Prediction of Melt Pool Depth and Dilution in Laser Powder Deposition," *Journal of Physics D: Applied Physics*, Vol. **39**(12), pp. 2613-2623.

- [61] Lin, J., 1999, "A Simple Model of Powder Catchment in Coaxial Laser Cladding," *Optics and Laser Technology*, Vol. **31**(3), pp. 233-238.
- [62] Chande, T., and Mazumber, J., 1985, "Two-Dimensional, Transient Model for Mass Transport in Laser Surface Alloying," *Journal of Applied Physics*, Vol. **57**(6), pp. 2226-2232.
- [63] Qi, H., and Mazumber, J., 2006, "Numerical Simulation of Heat Transfer and Fluid Flow in Coaxial Laser Cladding Process for Direct Metal Deposition," *Journal of Applied Physics*, Vol. **100**(2), pp. 024903.